



HAL
open science

Grafting of Anionic Decahydro-Closo-Decaborate Clusters on Keggin and Dawson-Type Polyoxometalates: Syntheses, Studies in Solution, DFT Calculations and Electrochemical Properties

Manal Diab, Ana C. Mateo, Jomada El Cheikh, Zeinab El Hajj, Mohamed Haouas, Alireza Ranjbari, Vincent Guérineau, David Touboul, Nathalie Leclerc, Emmanuel Cadot, et al.

► To cite this version:

Manal Diab, Ana C. Mateo, Jomada El Cheikh, Zeinab El Hajj, Mohamed Haouas, et al.. Grafting of Anionic Decahydro-Closo-Decaborate Clusters on Keggin and Dawson-Type Polyoxometalates: Syntheses, Studies in Solution, DFT Calculations and Electrochemical Properties. *Molecules*, 2022, 27 (22), 10.3390/molecules27227663 . hal-03888940

HAL Id: hal-03888940

<https://hal.science/hal-03888940>

Submitted on 14 Dec 2022

HAL is a multi-disciplinary open access archive for the deposit and dissemination of scientific research documents, whether they are published or not. The documents may come from teaching and research institutions in France or abroad, or from public or private research centers.







L'archive ouverte pluridisciplinaire **HAL**, est destinée au dépôt et à la diffusion de documents scientifiques de niveau recherche, publiés ou non, émanant des établissements d'enseignement et de recherche français ou étrangers, des laboratoires publics ou privés.



Distributed under a Creative Commons Attribution 4.0 International License

Article

Grafting of Anionic Decahydro-*Closo*-Decaborate Clusters on Keggin and Dawson-Type Polyoxometalates: Syntheses, Studies in Solution, DFT Calculations and Electrochemical Properties

Manal Diab ^{1,2}, Ana Mateo ³ , Joumada El Cheikh ⁴, Zeinab El Hajj ^{1,2}, Mohamed Haouas ¹ , Alireza Ranjbari ⁵ , Vincent Guérineau ⁶, David Touboul ⁶ , Nathalie Leclerc ¹, Emmanuel Cadot ¹, Daoud Naoufal ^{2,*} , Carles Bo ^{2,*}  and Sébastien Floquet ^{1,*}

¹ Institut Lavoisier de Versailles, CNRS, UVSQ, Université Paris-Saclay, 78035 Versailles, France

² Laboratory of Organometallic and Coordination Chemistry, LCIO, Faculty of Sciences I, Lebanese University, Hadath 6573, Lebanon

³ Institute of Chemical Research of Catalonia (ICIQ), The Barcelona Institute of Science and Technology, 43007 Tarragona, Spain

⁴ Equipe de Recherche et Innovation en Electrochimie pour l'énergie (ERIEE), Institut de Chimie Moléculaire et des Matériaux d'Orsay (ICMMO), UMR CNRS 8182, Université Paris-Sud, Université Paris-Saclay, 91405 Orsay, France

⁵ Institut de Chimie Physique, CNRS, UMR 8000, Université Paris-Saclay, 91405 Orsay, France

⁶ Institut de Chimie des Substances Naturelles, CNRS UPR2301, Université Paris-Sud, Université Paris-Saclay, 91198 Gif-sur-Yvette, France

* Correspondence: dnaoufal@ul.edu.lb (D.N.); cbo@icqi.cat (C.B.); sebastien.floquet@uvsq.fr (S.F.)



Citation: Diab, M.; Mateo, A.; El Cheikh, J.; El Hajj, Z.; Haouas, M.; Ranjbari, A.; Guérineau, V.; Touboul, D.; Leclerc, N.; Cadot, E.; et al. Grafting of Anionic Decahydro-*Closo*-Decaborate Clusters on Keggin and Dawson-Type Polyoxometalates: Syntheses, Studies in Solution, DFT Calculations and Electrochemical Properties. *Molecules* **2022**, *27*, 7663. <https://doi.org/10.3390/molecules27227663>

Academic Editor: Xiaobing Cui

Received: 2 October 2022

Accepted: 2 November 2022

Published: 8 November 2022

Publisher's Note: MDPI stays neutral with regard to jurisdictional claims in published maps and institutional affiliations.



Copyright: © 2022 by the authors. Licensee MDPI, Basel, Switzerland. This article is an open access article distributed under the terms and conditions of the Creative Commons Attribution (CC BY) license (<https://creativecommons.org/licenses/by/4.0/>).

Abstract: Herein we report the synthesis of a new class of compounds associating Keggin and Dawson-type Polyoxometalates (POMs) with a derivative of the anionic decahydro-*closo*-decaborate cluster $[B_{10}H_{10}]^{2-}$ through aminopropylsilyl ligand (APTES) acting as both a linker and a spacer between the two negatively charged species. Three new adducts were isolated and fully characterized by various NMR techniques and MALDI-TOF mass spectrometry, notably revealing the isolation of an unprecedented monofunctionalized SiW_{10} derivative stabilized through intramolecular H-H dihydrogen contacts. DFT as well as electrochemical studies allowed studying the electronic effect of grafting the decaborate cluster on the POM moiety and its consequences on the hydrogen evolution reaction (HER) properties.

Keywords: polyoxometalate; hybrid; decaborate; DFT; NMR; hydrogen evolution reaction

1. Introduction

Polyoxometalates (POMs) and POM-based materials constitute a highly versatile class of compounds rich in more than several thousand inorganic compounds, which can be finely tuned at the molecular level. Because of their stunning compositions, diversified architectures and their rich electrochemical redox behaviors, they are known to display numerous properties or applications in many domains such as supramolecular chemistry [1–3], catalysis [4–6], electro-catalysis [7–9], and medicine, especially when POMs are functionalized with organic groups or complexes [10–13].

On their side, hydroborates represent a wide family of anionic clusters, for which many reports demonstrated their interest in different areas, especially in the biomedical domain [14–18]. This property thus makes the studies of borane derivatives of a great interest. In particular, the $[B_{10}H_{10}]^{2-}$ cluster offers the possibility of various selective functionalizations [19,20] leading for example to *closo*-decaborate-triethoxysilane precursor, which can be coordinated to luminescent dye doped silica nanoparticles, hence facilitating the tracing of the *closo*-decaborate drug pathway in BNCT (Boron Neutron Capture Therapy) [21,22].

Driven by the synthetic challenge that constitutes the association of two anionic species with two complementary redox characters, reductive for hydroborates and oxidative for POMs, and by the biomedical applications which could be reached by associating these two families of compounds, this study aims to find the right strategy to design such POM-borate adducts and to study their chemical properties.

In a previous paper, we demonstrated that it is possible to covalently graft decaborate clusters to an Anderson-type polyoxometalate functionalized with the well-known TRIS ligand (TRIS = tris(hydroxymethyl)aminomethane), namely $[\text{Mn}^{\text{III}}\text{Mo}_6\text{O}_{18}(\text{TRIS})_2]^{3-}$ [23]. Nevertheless, the compound $[\text{Mn}^{\text{III}}\text{Mo}_6\text{O}_{18}(\text{TRIS-B}_{10})_2]^{7-}$ resulting from the coupling between both components revealed to be fragile, probably because of the rigidity of the linker and the close proximity of both anionic components. This weakness is confirmed by DFT calculations indicating an athermic or slightly exothermic process for the formation of the adducts with Anderson-TRIS hybrid POMs.

In the field of hybrid POMs, the organosilyl derivatives of vacant polyoxotungstates as $[\text{PW}_9\text{O}_{34}]^{9-}$, $[\text{SiW}_{10}\text{O}_{36}]^{8-}$, $[\text{PW}_{11}\text{O}_{39}]^{7-}$, $[\text{SiW}_{11}\text{O}_{39}]^{6-}$, or $[\text{P}_2\text{W}_{17}\text{O}_{61}]^{10-}$ offer large diversities of compounds exhibiting a wide panel of applications [24,25]. Among them, the divacant POM Keggin $[\text{SiW}_{10}\text{O}_{36}]^{8-}$ (noted hereafter SiW_{10}) and the monovacant POM Dawson $[\text{P}_2\text{W}_{17}\text{O}_{61}]^{10-}$ (noted hereafter P_2W_{17}) derivatives are probably the most used because of their stability, their topology and the richness of their electrochemical properties in reduction. In particular, by reacting with aminopropyltri(ethoxy)silane (called APTES) they can provide two very useful platforms, noted respectively $\text{SiW}_{10}\text{-APTES}$ and $\text{P}_2\text{W}_{17}\text{-APTES}$ (see Figure 1), for elaborating functional hybrid molecular architectures.

The aim of this study is to use these two different platforms to prepare new hybrid compounds associating an anionic decaborate boron cluster (denoted hereafter B_{10}) with Keggin and Dawson POM derivatives. The choice of polyoxotungstate moieties rather than Mo-based POMs is based on its stability towards reduction. The employment of a long and flexible linker as APTES is essential to tackle the challenge of combining efficiently a reduced anionic boron cluster with an anionic oxidized polyoxometalate. The use of APTES linker should limit the repulsion between the two components, while its flexibility allows more easily accommodating the two entities. Finally, as shown in Figure 1, due to monovacant and divacant characters of P_2W_{17} and SiW_{10} , respectively, it is worth noting that the relative conformations of the chains are different. For $\text{SiW}_{10}\text{-APTES}$, the two alkyl chains are oriented nearly in parallel, whereas the monovacancy of P_2W_{17} imposes divergent directions for the two alkyl chains. This topology is well adapted for designing triangular or square molecular species as evidenced by Izzet et al. [2,26], and in our case, we expect that these two kinds of conformation could lead to different types of adducts incorporating B_{10} clusters. In this study, we thus report the synthesis, the full characterization in solution by various NMR techniques, the electronic, the electrochemical and the electrocatalytic properties of three new hybrid POMs. In the absence of XRD structures, DFT studies provide a fine structural description of these hybrids and rationalization of their properties.

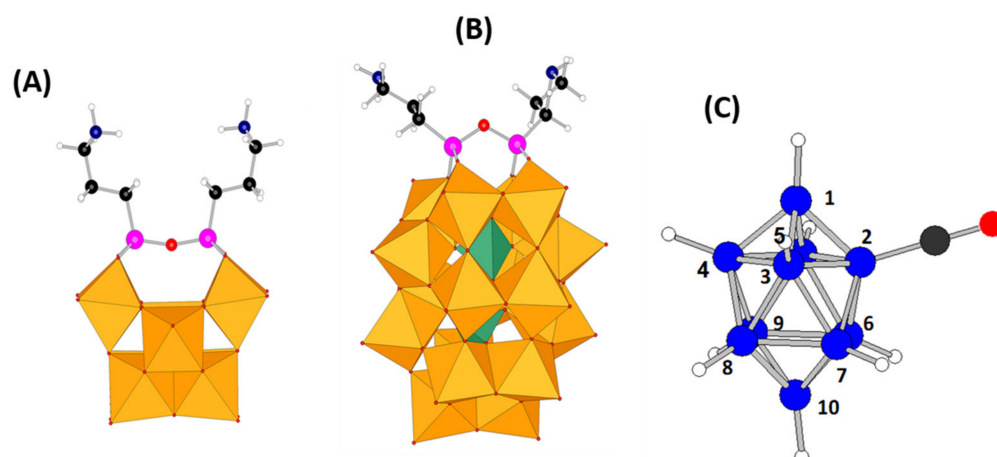


Figure 1. Molecular structures (DFT-optimized geometry) of (A) SiW_{10} -APTES and (B) P_2W_{17} -APTES platforms highlighting the two different topologies of the APTES linker, and of (C) $[\text{B}_{10}\text{H}_9\text{CO}]^-$ (X-ray diffraction structure from reference [27]). Legend: C in black, H in white, N in dark blue, Si in pink, O in red, B in blue, WO_6 octahedra in orange and PO_4 tetrahedra in green.

2. Results and Discussion

2.1. Syntheses

The synthesis of hybrid POMs can be achieved through different strategies. In the present study, the best synthetic procedure to get the targeted hybrid POMs has been to react first the lacunary POMs “ SiW_{10} ” and “ P_2W_{17} ” with two aminopropyltri(ethoxy)silane molecules (APTES) to give the two POM-APTES precursors (see Figure 2) of formulas $(\text{TBA})_3\text{H}[(\text{SiW}_{10}\text{O}_{36})(\text{Si}(\text{CH}_2)_3\text{NH}_2)_2\text{O}]\cdot 3\text{H}_2\text{O}$ (denoted hereafter SiW_{10} -APTES) and $(\text{TBA})_5\text{H}[\text{P}_2\text{W}_{17}\text{O}_{61}(\text{Si}(\text{CH}_2)_3\text{NH}_2)_2\text{O}]\cdot 6\text{H}_2\text{O}$, denoted hereafter P_2W_{17} -APTES. The syntheses of these two precursors were adapted from Mayer et al. [28] by reaction of $\text{k}_8(\gamma\text{-SiW}_{10}\text{O}_{36})\cdot 12\text{H}_2\text{O}$ or $\text{K}_{10}\alpha\text{-P}_2\text{W}_{17}\text{O}_{61}\cdot 20\text{H}_2\text{O}$ with 3-aminopropyltriethoxy silane in presence of TBABr in $\text{H}_2\text{O}/\text{CH}_3\text{CN}$ medium acidified by concentrated HCl (for more details see experimental section in Supplementary Materials). Note that for each, the proton usually written as counter-cation is in fact probably an ammonium arm R-NH_3^+ .

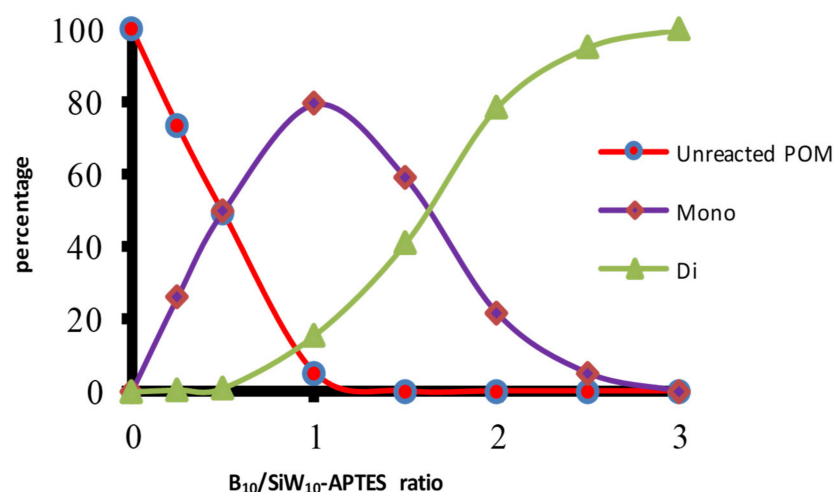


Figure 2. Evolution of the proportions of the products in the system SiW_{10} -APTES/ $\text{B}_{10}\text{H}_9\text{CO}$ /DIPEA as a function of $\text{B}_{10}\text{H}_9\text{CO}/\text{SiW}_{10}$ -APTES ratio at fixed DIPEA/ $\text{B}_{10}\text{H}_9\text{CO}$ ratio of 2. The proportion of each species are determined by integration of the ^{29}Si NMR signals. Reproduced with permission from the doctoral thesis manuscript of Dr Manal Diab, University Paris Saclay/Lebanese University, May 2018.

The synthetic strategy to get POM-borate adducts is then to combine the amines of these POM-APTES precursors with the reactive carbonyl of the decaborate cluster $[B_{10}H_9CO]^-$ (Figure 1C) to give an amide function connecting both components. Since the boron cluster can react with water for giving a carboxylic acid and since heating the synthetic mixture above 40–50 °C led to some degradation products or to some reduction in the Dawson derivative by the hydrodecaborate cluster, reactions have been conducted at room temperature and under nitrogen atmosphere. Furthermore, the coupling reaction needs the presence of a base both to help the deprotonation of the ammonium arm(s) of the POM-APTES precursors and to trap the proton produced by the coupling reaction. A moderate and a bulky organic base, diisopropylethylamine (DIPEA), was thus used to avoid the competition with APTES for the coupling reaction with $[B_{10}H_9CO]^-$.

To quickly circumscribe the optimal conditions for the synthesis of the POM-borate adducts, ^{29}Si , ^{31}P and 1H NMR titrations were conducted by varying the ratios of the three reactants $[B_{10}H_9CO]^-$ / POM-APTES / DIPEA (all details are given in the Supplementary Materials).

For the $[B_{10}H_9CO]^-$ / **SiW₁₀-APTES** / DIPEA system, the ^{29}Si NMR studies in solution reveal that it is possible to modulate the coupling reaction between $[B_{10}H_9CO]^-$ and POM-APTES precursors by playing on the amounts of DIPEA and of $[B_{10}H_9CO]^-$. For this tri-reactants system, the successive formation of two POM-borate species identified as mono- and di-adduct compounds was demonstrated thanks to their molecular symmetries (C_s versus C_{2v}). Besides, the crucial role of DIPEA in the reaction of $[B_{10}H_9CO]^-$ with POM-APTES precursors was clearly evidenced. No reaction occurs when no base is used. NMR titration studies allowed establishing that the optimal quantity of base was two equivalents for one equivalent of $[B_{10}H_9CO]^-$. The Figure 2 shows for instance the proportions of **SiW₁₀**-derivatives determined by the integration of the different peaks obtained by ^{29}Si NMR in the system **SiW₁₀-APTES** / $[B_{10}H_9CO]^-$ / DIPEA as a function of $[B_{10}H_9CO]^-$ / **SiW₁₀-APTES** ratio at fixed DIPEA / $[B_{10}H_9CO]^-$ ratio of 2.

Starting from **SiW₁₀-APTES**, it evidences first the formation of a mono-adduct, which predominates for ration $B_{10} / \text{SiW}_{10}\text{-APTES} = 1$, before being converted into a di-adduct. The NMR titrations studies allowed establishing that using proportions **SiW₁₀-APTES** / $B_{10}H_9CO$ / DIPEA = 1/3/6 lead to the pure di-adduct denoted **SiW₁₀-diB₁₀**, while using 1/1/2 ratios lead to around 80% of mono-adduct mixed with some unreacted starting POM and the di-adduct. The separation of compounds has not been possible but considering the effect of the added DIPEA amounts, we succeeded to reduce the formation of the di-adduct and thus to get the mono-adduct compound denoted **SiW₁₀-monoB₁₀** with a good purity by decreasing the quantity of DIPEA in the proportions **SiW₁₀-APTES** / $B_{10}H_9CO$ / DIPEA = 1/1/1.5. The Figure 3 summarizes the experimental conditions used to isolate POM-borate adducts.

Similar NMR studies were also performed in solution with the Dawson derivative **P₂W₁₇-APTES** (see Supplementary Materials). In contrast to **SiW₁₀** derivatives, the formation of mono- and di-adduct of the Dawson derivative are not so separated as for **SiW₁₀**. Therefore, we failed to isolate the mono-adduct as pure product. Nevertheless, we can obtain quantitatively the di-adduct compound in the reaction mixture when ratios **P₂W₁₇-APTES** / $B_{10}H_9CO$ / DIPEA = 1/3/6 are used.

To summarize, the multistep coupling reactions have successfully been monitored by ^{29}Si and ^{31}P NMR, fully described in the Supplementary Materials, revealing that intermediate products can be followed and isolated. From these results, we established the experimental conditions allowing to selectively synthesize with good yields the mono adduct of **SiW₁₀** POM and the di-adducts of both POMs as mixed TBA^+ and $DIPEAH^+$ salts, namely $(TBA)_3(DIPEAH)_3[(SiW_{10}O_{36})(B_{10}H_9CONHC_3H_6Si)(NH_2C_3H_6Si)O] \cdot 3H_2O$ denoted **SiW₁₀-monoB₁₀**, $(TBA)_{6.5}(DIPEAH)_{1.5}[(SiW_{10}O_{36})(B_{10}H_9CONHC_3H_6Si)_2O] \cdot 2H_2O$ denoted **SiW₁₀-diB₁₀**, and $(TBA)_6(DIPEAH)_4[(P_2W_{17}O_{61})(B_{10}H_9CONHC_3H_6Si)_2O] \cdot 3H_2O$, denoted **P₂W₁₇-diB₁₀** (See Experimental Section in Supplementary Materials for more details). All adducts were isolated as powders and were characterized by FT-IR, TGA, elemental analysis, MALDI-TOF and NMR techniques. It should be noted that to our knowledge, **SiW₁₀**-

monoB₁₀ is the first example of a POM-APTES monoadduct isolated so far from the direct synthesis. All studies in the literature usually reported di-adducts with such types of hybrid POMs [29–31].

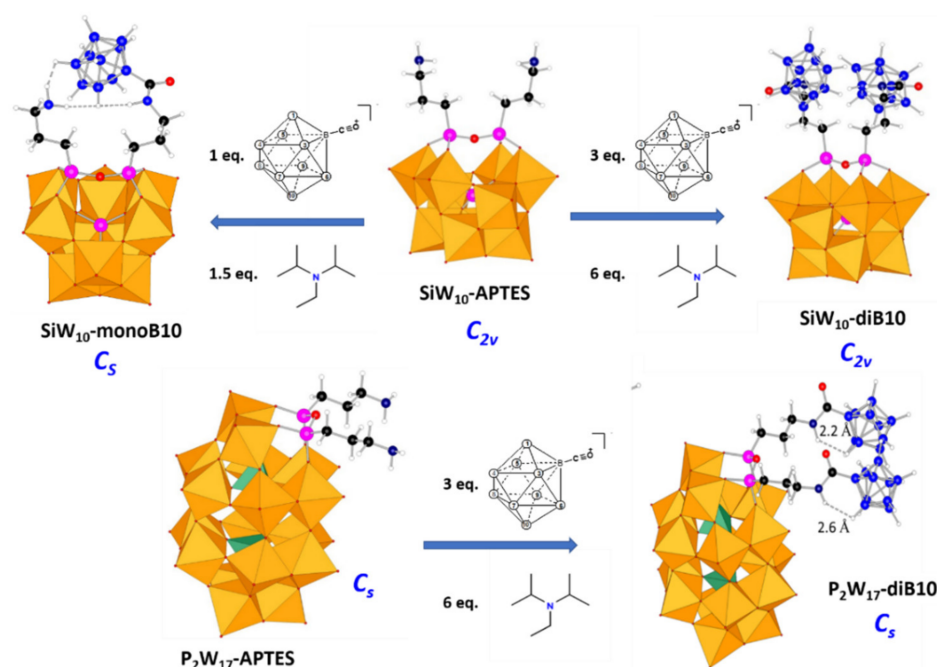


Figure 3. Scheme of syntheses of POM-borates adducts. The optimal quantities of reactants were determined by NMR titration studies. The reactions are performed in dry acetonitrile, at room temperature under inert atmosphere. Molecular structures are optimized geometry obtained by DFT. Legend: C in black, H in white, N in dark blue, Si in pink, O in red, B in blue, WO₆ octahedra in orange and PO₄ tetrahedra in green.

2.2. FT-IR Spectroscopy

FT-IR spectra are given in Figures S11 and S12 in Supplementary Materials. The FT-IR spectra of **SiW₁₀-monoB₁₀**, **SiW₁₀-diB₁₀** and **P₂W₁₇-diB₁₀** evidence that the integrity of the POM part is maintained compared to the POM-APTES precursors. Furthermore, the association of the [B₁₀H₉CO][−] cluster is demonstrated by the disappearance of the carbonyl CO band at 2098 cm^{−1} in the B₁₀H₉CO[−] cluster, while the broad band located at 2464–2470 cm^{−1} typical for B-H vibration bands of the decaborate moiety within the three compounds **SiW₁₀-monoB₁₀**, **SiW₁₀-diB₁₀** and **P₂W₁₇-diB₁₀** is significantly shifted from that observed at 2517 cm^{−1} for the [B₁₀H₉CO][−] precursor [22,23].

2.3. Characterizations by MALDI-TOF Mass Spectrometry

Mass spectrometry (MS) is a very efficient technique for the characterization of polyoxometalates in solution. In our case, we did not succeed in getting mass spectra with reasonable signal-to-noise ratio and exploitable data by the usual electrospray ESI-MS technique. On the contrary, Matrix-Assisted Laser Desorption/Ionization coupled to a Time-of-Flight mass spectrometer (MALDI-TOF) revealed to be an effective technique for hybrid POMs characterization, as shown for example by Mayer and coworkers on “SiW₁₀” and “P₂W₁₇” organosilyl derivatives [28,32]. MALDI-TOF technique is applied on samples which are diluted in a matrix solution (DCTB in our case, DCTB = Trans-2-[3-(4-ter-Butylphenyl)-2-propenylidene] malonitrile) and then co-crystallized on a conductive target. Thanks to a laser irradiation, it allows producing singly charged species (cationic or anionic) and presenting the great advantage to strongly limit the number of peaks in comparison with ESI-MS spectra, where multiply charged species are generated. In the present study, the experiments were performed in both negative and positive modes (see Figure S14 in the

Supplementary Materials for the example of $\text{SiW}_{10}\text{-diB}_{10}$). According to previous works in this field, the best results were obtained in the positive mode, although the anionic character of the POM [28,32]. Indeed, as seen in the Supplementary Materials for $\text{SiW}_{10}\text{-diB}_{10}$, the intensity reached in the negative mode appears lower, but the number of peaks is higher as there are more degradation species. Even though our systems are polyanionic, they are more efficiently analyzed as monocationic species resulting from adducts between POMs and counter cations such as TBA^+ and H^+ in our case (H^+ coming notably from DIPEAH^+ cations or protonated amines). Furthermore, the monocationic character of the species is confirmed in all cases by the shift between peaks in the isotopic massifs.

The precursor $\text{SiW}_{10}\text{-APTES}$ and the compounds $\text{SiW}_{10}\text{-monoB}_{10}$, $\text{SiW}_{10}\text{-diB}_{10}$ and $\text{P}_2\text{W}_{17}\text{-diB}_{10}$, were thus analyzed by this technique in the positive mode. The results are gathered in Table S1 (see Supplementary Materials). The full spectra and a zoom on the target compounds with a spectrum simulated with IsoPro3 software are shown in Figure 4 for SiW_{10} derivatives and in Figures S15 and S16 for P_2W_{17} ones.

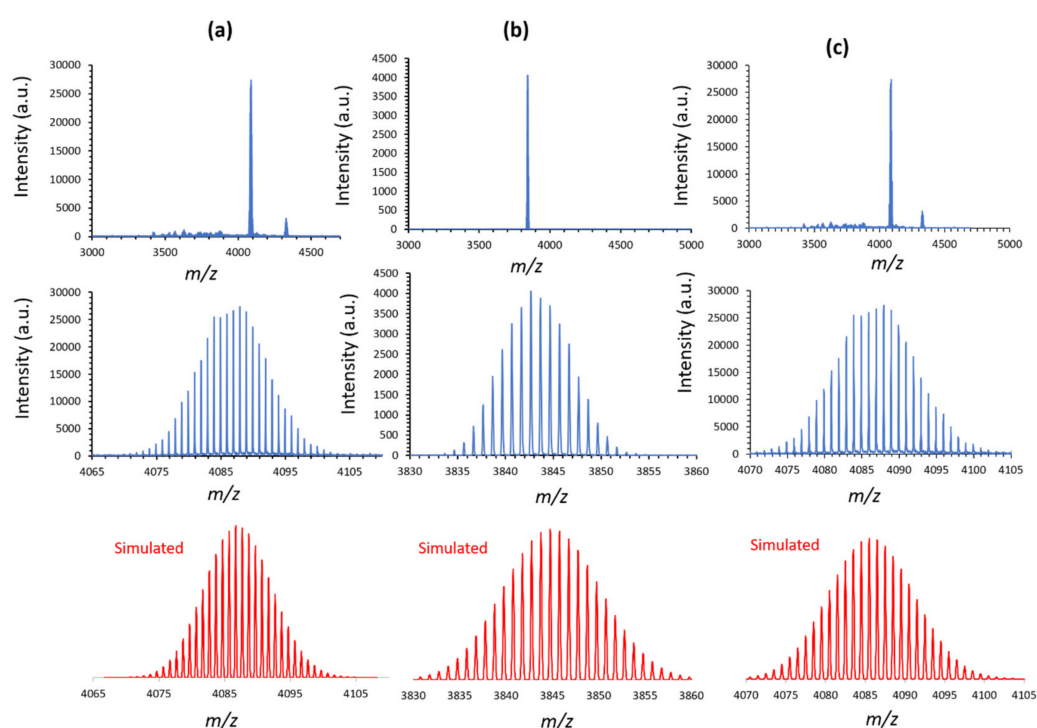


Figure 4. Reflector positive ion MALDI-TOF spectra of (a) $\text{SiW}_{10}\text{-APTES}$, (b) $\text{SiW}_{10}\text{-monoB}_{10}$, and (c) $\text{SiW}_{10}\text{-diB}_{10}$. Zooms of major peaks in the 3000–5000 m/z range are displayed with their respective simulated spectra.

As shown in Figure 4 the spectrum of the precursor $\text{SiW}_{10}\text{-APTES}$ (Figure 4a) displays a major peak centered at m/z 4087.3 and a minor peak at m/z 4328.3. The first peak is assigned to the monocationic species $\{(\text{TBA})_3\text{H}_2[(\text{SiW}_{10}\text{O}_{36})\text{O}(\text{SiC}_3\text{H}_6\text{NH}_2)_2](\text{CH}_3\text{CN})_2(\text{H}_2\text{O})_8(\text{DCTB})_2\}^+$ (calculated m/z 4087.3), while the second peak is attributed to the species $\{(\text{TBA})_4\text{H}[(\text{SiW}_{10}\text{O}_{36})\text{O}(\text{SiC}_3\text{H}_6\text{NH}_2)_2](\text{CH}_3\text{CN})_2(\text{H}_2\text{O})_8(\text{DCTB})_2\}^+$ (calculated m/z 4328.7). The two peaks correspond to the expected hybrid POM associated with some TBA^+ and H^+ cations, some solvates and two molecules of the DCTB matrix. Note that the presence of amines on the APTES part of the POM could probably favor the formation of intermolecular interactions with solvates and DCTB molecules. Such an adduct with DCTB is also observed with the precursor $\text{P}_2\text{W}_{17}\text{-APTES}$ (Figure S15, Supplementary Materials) but not seen with the other POMs functionalized with B_{10} clusters. The MALDI-TOF spectrum of $\text{P}_2\text{W}_{17}\text{-APTES}$ indeed exhibits a major peak corresponding to the expected precursor associated with one molecule of the DCTB matrix at m/z 6058.7 (calculated m/z 6057.9 for $(\text{TBA})_6\text{H}[(\text{P}_2\text{W}_{17}\text{O}_{61})\text{O}(\text{SiC}_3\text{H}_6\text{NH}_2)_2](\text{DCTB})\}^+$) and a minor peak at m/z 6300.0

(calculated m/z 6299.4 for $(\text{TBA})_7[(\text{P}_2\text{W}_{17}\text{O}_{61})\text{O}(\text{SiC}_3\text{H}_6\text{NH}_2)_2](\text{DCTB})\}^+$). The attribution of the peaks is definitely confirmed thanks to the fitting of the isotopic distribution massifs. The latter are mainly due to the isotopic distribution of the 10 or 17 tungsten atoms of the POMs, which appears consistent with the experimental spectrum (see Figure 4a and Figure S15, respectively).

The spectrum of **SiW₁₀-monoB₁₀** depicted in Figure 4b shows only one experimental peak at m/z 3843.2 which is perfectly consistent with the calculated mass for the monocationic product $\{(\text{TBA})_4\text{H}_3[(\text{SiW}_{10}\text{O}_{36})\text{O}(\text{SiC}_3\text{H}_6\text{NH}_2)(\text{SiC}_3\text{H}_6\text{NHC}\text{O}\text{B}_{10}\text{H}_9)](\text{CH}_3\text{CN})(\text{H}_2\text{O})_3\}^+$ (calculated m/z 3843.1). It evidences the formation of the expected adduct **SiW₁₀-monoB₁₀** and thus indirectly the grafting of one $(\text{B}_{10}\text{H}_9\text{CO})^-$ cluster to **SiW₁₀-APTES**. The simulated spectrum agrees well with the experimental data, which supports this assumption although the presence of one B_{10} cluster does not modify significantly the isotopic massif.

The MALDI-TOF spectrum of **SiW₁₀-diB₁₀** shown in Figure 4c displays a major peak centered at m/z 4085.8, which fully agrees with the expected di-grafted compound $\{(\text{TBA})_4\text{H}_5[(\text{SiW}_{10}\text{O}_{36})\text{O}(\text{SiC}_3\text{H}_6\text{NHC}\text{O}\text{B}_{10}\text{H}_9)_2](\text{CH}_3\text{CN})_2(\text{H}_2\text{O})_6\}^+$ (m/z calculated 4084.4) and a minor peak at $m/z = 4330.2$ consistent with the species $\{(\text{TBA})_5\text{H}_4[(\text{SiW}_{10}\text{O}_{36})\text{O}(\text{SiC}_3\text{H}_6\text{NHC}\text{O}\text{B}_{10}\text{H}_9)_2](\text{CH}_3\text{CN})_3(\text{H}_2\text{O})_4\}^+$ (m/z calculated 4330.8). This result confirms the formation of the expected di-grafted compound.

Finally, the case of **P₂W₁₇-diB₁₀**, appears more complicated, certainly due to a higher charge of the hybrid POM (10-) and a larger surface, which both favor intermolecular interactions with solvent molecules and cations. For technical reasons, the MALDI-TOF spectrum shown in Figure S16 (see Supplementary Materials) was recorded in linear mode, which does not favor the high resolution in contrast with other compounds. The spectrum displays an intense and broad experimental peak centered at m/z 6048.1, while four smaller peaks are found, respectively, at m/z 6289.6, 6431.7, 6672.5 and 6813.8. All these peaks are consistent with di-grafted species of general formula $\{(\text{TBA})_x\text{H}_y[(\text{P}_2\text{W}_{17}\text{O}_{61})\text{O}(\text{SiC}_3\text{H}_6\text{NHC}\text{O}\text{B}_{10}\text{H}_9)_2](\text{CH}_3\text{CN})_z(\text{H}_2\text{O})_t\}^+$ ($x + y = 11$, $z = 0-3$ and $t = 5-6$). Regarding the main peak, the latter appears much broader than expected for only one species. Moreover, the resolution of the isotopic massif is lost. In fact, the experimental spectrum likely corresponds to a spectra superimposition of monocationic species of general formula $\{(\text{TBA})_5\text{H}_6[(\text{P}_2\text{W}_{17}\text{O}_{61})\text{O}(\text{SiC}_3\text{H}_6\text{NHC}\text{O}\text{B}_{10}\text{H}_9)_2](\text{CH}_3\text{CN})_x(\text{H}_2\text{O})_y\}^+$ with x ranging from 1 to 5 and y from 0 to 8 (m/z in the range 6035.70 to 6076.75). Some simulated spectra are given in Figure S16 in Supplementary Materials.

2.4. NMR Studies in Solution

In the absence of crystallographic data, the three obtained hybrid systems have been thoroughly characterized by multinuclear NMR spectroscopy in order to verify their structures in solution. ^1H , ^{11}B , ^{13}C , ^{15}N , ^{29}Si , ^{31}P , and ^{183}W NMR spectra were recorded in CD_3CN at room temperature. The data are gathered in Table S2 (Supplementary Materials), while selected spectra are given in Figures 5 and 6 and in Figures S17–S32 (Supplementary Materials).

As shown in Figure 5a and in Figures S17–S20 (Supplementary Materials), $^{11}\text{B}\{^1\text{H}\}$ NMR spectrum of $[\text{B}_{10}\text{H}_9\text{CO}]^-$ undergoes a significant change upon coupling with **SiW₁₀-APTES** or **P₂W₁₇-APTES**. In particular, the signal at -44.4 ppm specific for the equatorial boron atom bearing the substituent CO in $[\text{B}_{10}\text{H}_9\text{CO}]^-$ (B2 atom, see Figure 1c) is strongly shifted to ca. -25 ppm in the spectra of **SiW₁₀-monoB₁₀**, **SiW₁₀-diB₁₀** and **P₂W₁₇-APTES** in agreement with the grafting of the cluster on the POM.

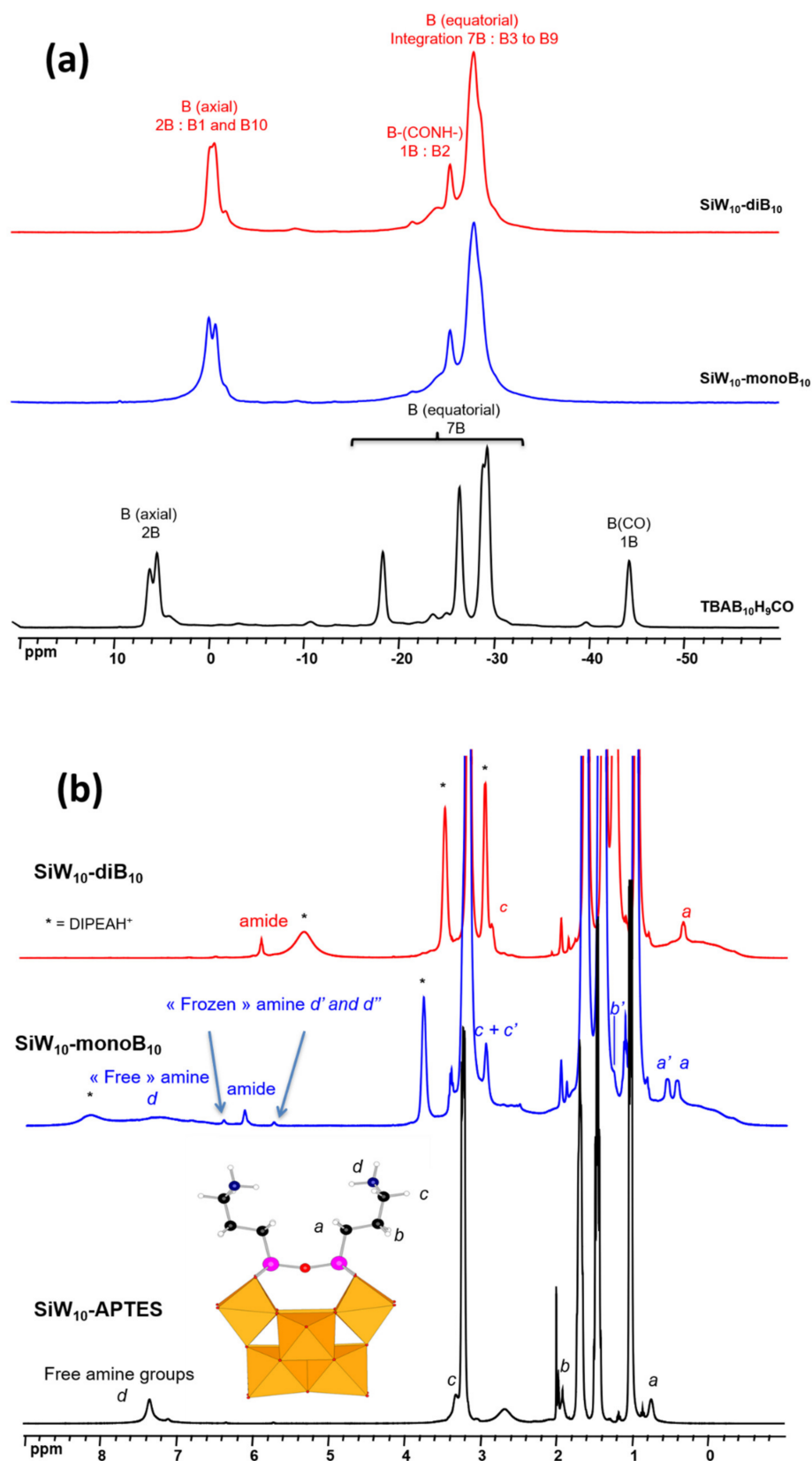


Figure 5. (a) $^{11}\text{B}\{^1\text{H}\}$ NMR spectra of $\text{SiW}_{10}\text{-monoB}_{10}$, $\text{SiW}_{10}\text{-diB}_{10}$ and $\text{TBA}[\text{B}_{10}\text{H}_9\text{CO}]$ in CD_3CN . (b) ^1H NMR spectra of $\text{SiW}_{10}\text{-monoB}_{10}$, $\text{SiW}_{10}\text{-diB}_{10}$ and $\text{SiW}_{10}\text{-APTES}$ in CD_3CN . * indicates the signal of the protonated amine DIPEAH^+ present as a counter-cation. Reproduced with permission from the doctoral thesis manuscript of Dr Manal Diab, University Paris Saclay/Lebanese University, May 2018.

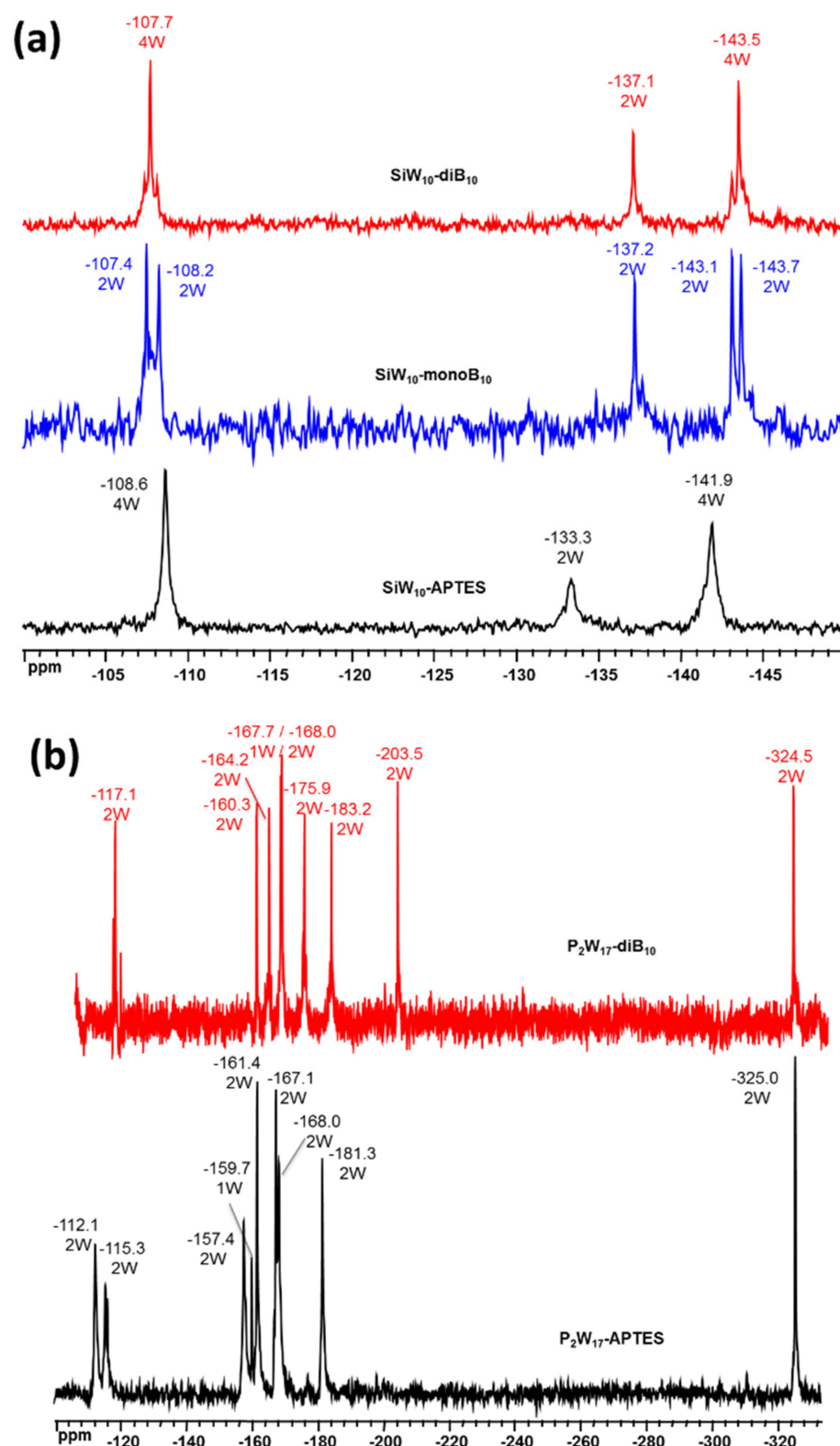


Figure 6. (a) ^{183}W NMR spectra of $\text{SiW}_{10}\text{-monoB}_{10}$, $\text{SiW}_{10}\text{-diB}_{10}$ and $\text{SiW}_{10}\text{-APTES}$ in CD_3CN . (b) ^{183}W NMR spectra of $\text{P}_2\text{W}_{17}\text{-diB}_{10}$ and $\text{P}_2\text{W}_{17}\text{-APTES}$ in CD_3CN .

Concomitantly, the ^1H NMR spectrum of the mono adduct $\text{SiW}_{10}\text{-monoB}_{10}$, exhibits a splitting of the signals for the three methylene groups $-\text{CH}_2-$ of the APTES linker, denoted a, b, c (see Figure 5b), because of the lowering of the symmetry of $\text{SiW}_{10}\text{-APTES}$ from C_{2v} to C_s . In addition, a new peak at 6.12 ppm assigned to an amide function is observed.

For the remaining amine function, a broad signal is observed at 7.4 ppm (d), but together with two other broad signals at 5.70 and 6.33 ppm (d' and d''), attributed to the amine function in a frozen configuration in which the interaction with B₁₀ cluster generates two inequivalent protons as depicted in Figure 7a (DFT optimized structure). These assumptions are confirmed by ¹H-¹⁵N HMBC (Heteronuclear Multiple Bond Correlation) NMR spectrum (Figure S25) revealing two ¹⁵N signals at −251 ppm (amide) correlated to the proton signal at 6.12 ppm and at −272 ppm (free amine) correlated to the two protons peaks at 5.70 and 6.33 ppm.

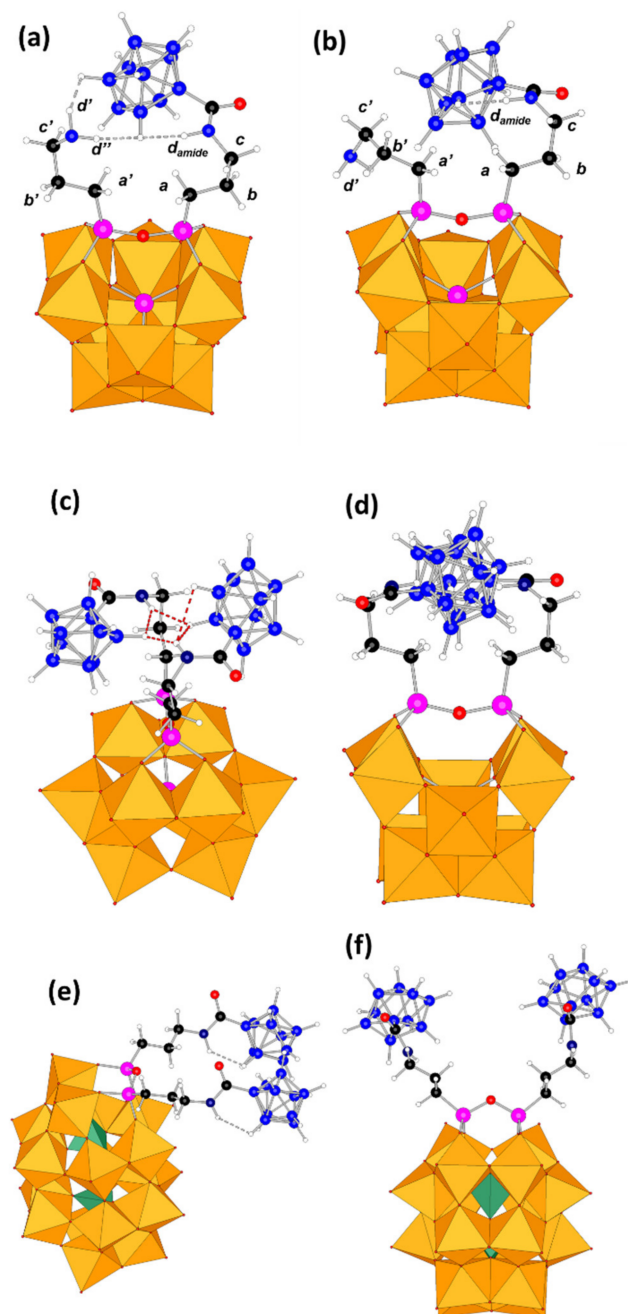


Figure 7. Optimized molecular structures of the POM-borates derivatives. **SiW₁₀-monoB₁₀** (a) in «closed» form and (b) in «open» form; (c,d) two views of the most stable configuration of **SiW₁₀-diB₁₀**; (e,f) two views of the most stable configuration of **P₂W₁₇-diB₁₀**. Dashed lines are given for shortest H-H contacts. Legend: C in black, H in white, B in blue, N in dark blue, Si in pink, WO₆ octahedra in orange and PO₄ tetrahedra in green.

Grafting a second $[B_{10}H_9CO]^-$ group on the **SiW₁₀-APTES** platform allows recovering the C_{2v} symmetry and thus one set of peaks was observed for the linker and especially the protons “a”, in addition to an amide peak at 5.94 ppm (Figure S24, Supplementary Materials). The signals of the amine at 7.4, 5.7, and 6.3 ppm disappear in agreement with the reaction of $[B_{10}H_9CO]^-$ groups with this function. Similarly, the 1H NMR spectrum of **P₂W₁₇-diB₁₀** compared to that of **P₂W₁₇-APTES** (Figure S27, Supplementary Materials) evidences the appearance of a sharp peak at 5.94 ppm assigned to an amide function, while the signal of the free amine at 7.03 ppm in the precursor **P₂W₁₇-APTES** disappears.

To further confirm our assignments of the signal of the amide function, 1H - 1H ROESY (Rotating frame Overhause Effect Spectroscopy) and ^{13}C NMR experiments were performed on **SiW₁₀-diB₁₀** and **P₂W₁₇-diB₁₀** (Figures S28–S32, Supplementary Materials). Cross REO peaks involving the amide proton (5.94 ppm in both compounds) and some equatorial B-H protons of the B_{10} cluster at 0.4 ppm and the protons “c” of the APTES chains can be seen in Figures S28 and S29 (Supplementary Materials). This demonstrates the spatial proximity between these protons that interact between each other through dipolar contacts. ^{13}C NMR spectra of **SiW₁₀-monoB₁₀**, **SiW₁₀-diB₁₀**, and **P₂W₁₇-diB₁₀** (Figures S30–S32) notably exhibits a signal at 203 ppm assigned to a carbon atom from an amide group, which is confirmed by 2D 1H - ^{13}C HMBC NMR spectrum of **SiW₁₀-monoB₁₀** evidencing a correlation between this ^{13}C signal at 203 ppm and the 1H amide signal at 6.12 ppm. Besides, in both cases of **SiW₁₀-monoB₁₀** and **SiW₁₀-diB₁₀** this ^{13}C signal appears as a poorly resolved quadruplet with a coupling constant of 95 Hz consistent with a $^1J_{13C-11B}$ coupling.

Therefore, 1H , 1H - ^{15}N HMBC, 1H - 1H ROESY, ^{13}C and 1H - ^{13}C HMBC NMR experiments unambiguously confirm the formation of an amide group in our three adducts by reaction of the amines of POM-APTES precursors with the carbonyl group of the cluster $[B_{10}H_9CO]^-$. The modification of the $^{11}B\{^1H\}$ NMR spectra of the boron cluster after its reaction with the POM-APTES precursors further confirms such results.

^{29}Si , ^{31}P and ^{183}W NMR probe the POM part in compounds **SiW₁₀-APTES**, **SiW₁₀-monoB₁₀**, **SiW₁₀-diB₁₀**, **P₂W₁₇-APTES** and **P₂W₁₇-diB₁₀** (see Figure 6 and Figures S21–S23 in Supplementary Materials). The unsymmetrical environment in the mono adduct **SiW₁₀-monoB₁₀** is clearly confirmed through the appearance of two peaks for Si of the different linker arms at -61.9 and -63.3 ppm, while only one signal was observed at -62.3 ppm for the symmetrical di adduct **SiW₁₀-diB₁₀** with only a small shift from the initial **SiW₁₀-APTES** precursor (-62.5 ppm). In addition, for all the compounds, a single peak is observed for the Si atom in the central cavity of the SiW_{10} POM moiety which is almost not affected by the grafting of the boron clusters and the resulting changes of symmetry of the adducts (Figure S21, Supplementary Materials). In case of **P₂W₁₇-APTES** and **P₂W₁₇-diB₁₀**, both compounds exhibit only one signal assigned to the two equivalent Si atoms of the APTES linker (Figure S22, Supplementary Materials).

The ^{183}W NMR spectra of precursors and adducts are given in Figure 6. For **SiW₁₀-monoB₁₀** the ^{183}W NMR spectrum displays five peaks of intensities 2:2:2:2:2 in agreement with the expected low C_s symmetry, while three resonances are observed for the di adduct **SiW₁₀-diB₁₀** and the initial precursor **SiW₁₀-APTES** of intensities (4:2:4) consistent with their C_{2v} symmetry (Figure 6a). Figure 6b shows the ^{183}W NMR spectrum of **P₂W₁₇-diB₁₀** which differs significantly from its precursor. Both compounds exhibit nine NMR lines of integration 2:2:2:1:2:2:2:2:2 in agreement with the expected C_s symmetry, but their positions are slightly changed. This is due to the modification of the P_2W_{17} moiety induced by the grafting of the two $[B_{10}H_9CO]^-$ clusters. Additionally, ^{31}P NMR spectra of **P₂W₁₇-APTES** and **P₂W₁₇-diB₁₀** display two signals (Figure S23, Supplementary Materials), wherein one of them showed a common chemical shift, while the second exhibited a small shift from -13.4 ppm in **P₂W₁₇-APTES** to -13.6 ppm in **P₂W₁₇-diB₁₀**.

In conclusion, these experiments focused on the POM part fully agree in terms of molecular symmetries with the formation of the expected mono- or di-adducts with B_{10} clusters.

2.5. Computational Studies

The molecular geometries of **SiW₁₀-APTES**, **SiW₁₀-monoB₁₀**, and **SiW₁₀-diB₁₀**, as well as those of **P₂W₁₇-APTES**, **P₂W₁₇-monoB₁₀** and **P₂W₁₇-diB₁₀** were fully optimized at a DFT level including implicit solvent effects (see Figure 7 and Supplementary Materials for computational details). We considered the most relevant plausible conformers. Firstly, regarding **SiW₁₀-APTES**, it exhibits two main conformers as defined by the orientation of the two amine organic arms, which we called them open and closed forms. The small difference in their relative energy, less than 1 kcal·mol⁻¹ in favor of the closed form (represented in Figure 1a), forecasted that further substitution would easily overcome any initial geometric preference in the reactants. Indeed, upon B₁₀ incorporation a much more complex situation arises. For **SiW₁₀-monoB₁₀** we characterized five conformers, two arising from the closed reactant and three species from the open reactant form. In the most stable conformer (Figure 7a), which arise from the closed form, the decaborate moiety interacts favorably with the amine hydrogens (d' and d'') of the unreacted arm through strong dihydrogen contacts. In the most stable open form (Figure 7b), although interaction between arms is almost neglected, the H amide atom develops other interactions. Overall, the most stable conformer given in Figure 7a is 11 kcal·mol⁻¹ below the second one (Figure 7b). All five conformers lie in a narrow 20 kcal·mol⁻¹ range. For the double substituted **SiW₁₀-diB₁₀**, since the additional repulsion arising from the negatively charged B₁₀ groups, we could only characterize two forms: an open (not shown) and a closed one (two views on Figure 7c,d). The energy difference between both species was computed to be just only 5 kcal·mol⁻¹. We highlight, as dashed lines in Figure 7, those hydrogen atoms of the organic arm and the B₁₀ moiety that lie close in three-dimensional space.

Due to the monovacant character of P₂W₁₇, the Si-O-Si angle of the APTES moiety grafted to the POM strongly differs from that observed for the divacant SiW₁₀ POM (see Figure 1). The topology of the two arms, and thus the connectivity of the two POM-APTES derivatives, strongly differs. Therefore, as seen in Figure 1, closed form is not possible for P₂W₁₇-APTES. Only one geometry could thus be considered. Then, for the mono-substituted P₂W₁₇-monoB₁₀, two conformers were characterized, one open and one folded, the folded one being more stable by only 2.2 kcal·mol⁻¹. For the di-substituted Dawson derivative, only one open shaped product could be characterized (see Figure 7e,f).

Hydrogen atoms of the decaborate moieties possess a hydride character. Consequently, they can establish hydrogen-hydrogen contacts with protic solvent or with functional groups like amines or amides. In the present structures, many H-H dihydrogen contacts between the amine organic arms from APTES moiety and hydrogen atoms from decaborate clusters were observed. For instance, for **SiW₁₀-monoB₁₀** (Figure 7a), the hydrogen atoms d' and d'' from the «free» amino group are found 2.21 and 1.99 Å far from an H atom belonging to the B₁₀ cluster, which are quite short distances. This fact agrees with the couplings observed in the NMR experiments.

The thermodynamics of the formation of the mono- and di-adducts of the Keggin and the Dawson species is computed exergonic in all cases as seen in Figure 8. For **SiW₁₀-APTES**, both the formation of the mono- and bi-derivative were computed exergonic, 22.1 kcal·mol⁻¹ for the **SiW₁₀-monoB₁₀**, and 13.0 kcal·mol⁻¹ for the **SiW₁₀-diB₁₀**. The formation of **SiW₁₀-monoB₁₀** is clearly favored and the strong dihydrogen contacts between amino group and the grafted B₁₀ cluster undoubtedly strongly stabilize such a species compared to the di-adduct **SiW₁₀-diB₁₀**. For P₂W₁₇-APTES, also the two substitutions are favorable, 6.8 kcal·mol⁻¹ for the first, and 7.9 kcal·mol⁻¹ for the second.

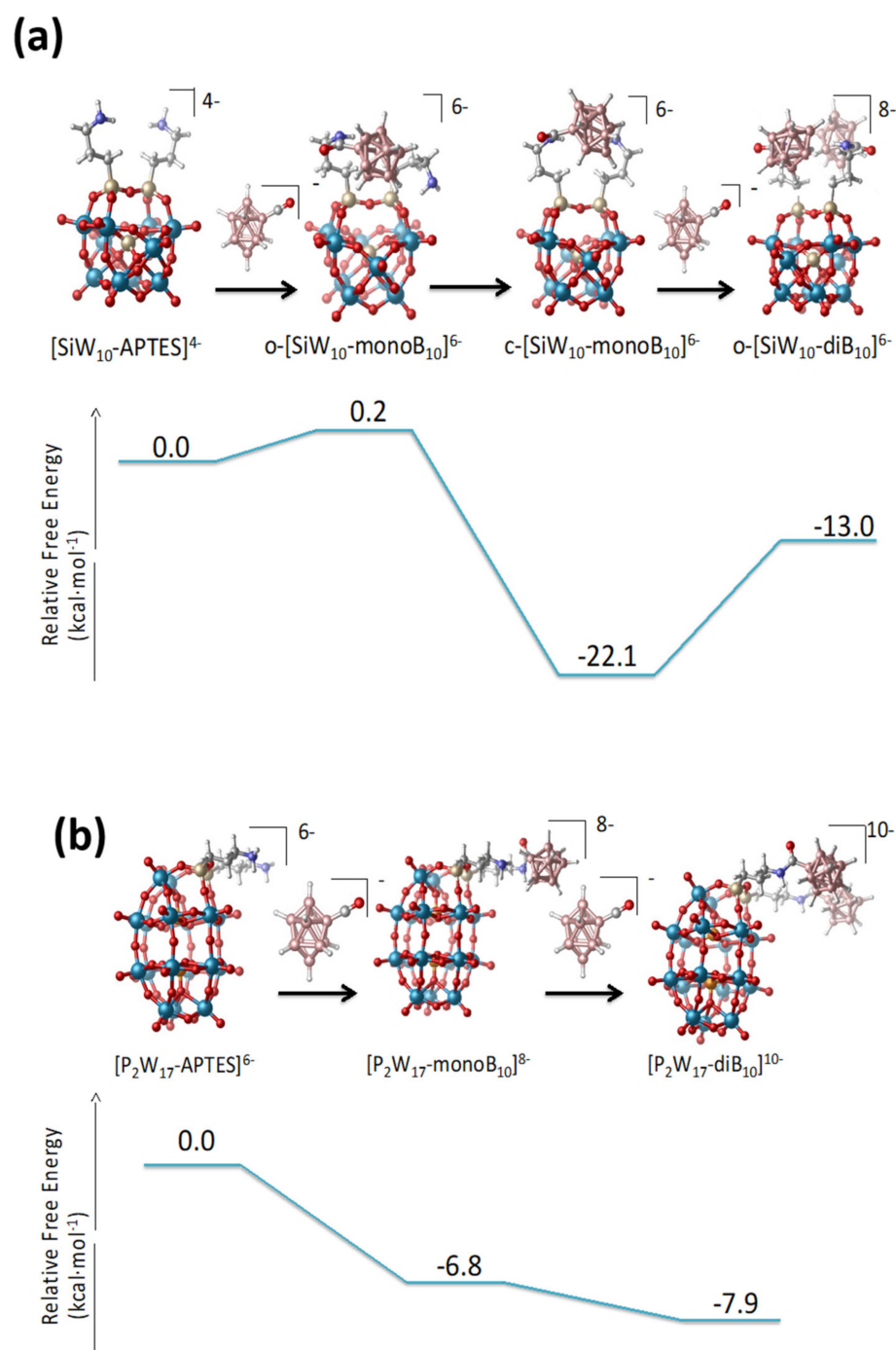


Figure 8. Energetic profiles of the formation of mono- and di-adduct from the starting precursors in CD₃CN. (a) SiW₁₀-APTES, SiW₁₀-monoB₁₀ (open and closed isomers), and SiW₁₀-diB₁₀; (b) P₂W₁₇-APTES, P₂W₁₇-monoB₁₀, and P₂W₁₇-diB₁₀.

The computed reaction free energies for the SiW₁₀-APTES and P₂W₁₇-APTES derivatives are fully consistent with the experimental findings. For the keggins derivatives, the strong stabilization of the mono-adduct allows isolating both mono and di-adduct thanks to the formation of strong H-H contacts. In contrast, for the Dawson derivatives, the small difference of energies between mono- and bi-adducts (1.1 eV only) does not permit isolating the mono-adduct. Besides, an excess of [B₁₀H₉CO]⁻ (3 equivalents/POM instead of 2) is needed to get the pure di-adduct compound to avoid the formation of a mixture between mono and di-grafted adducts. A similar situation was previously obtained with

Anderson-type derivatives since the mono and di-adduct of B_{10} with $[MnMo_6(Tris)_2]^{3-}$ are only separated by 6 eV and it was not possible to get mono-adduct [22]. This result highlights the role of the topology of the POM-APTES compounds and their faculty to stabilize species thanks to intramolecular interactions.

Finally, DFT studies provided the frontier orbitals for each compound (see Figure 9 and Figure S33 in Supplementary Materials). The results obtained for Keggin and Dawson derivatives exhibit the same feature. For POM-APTES the HOMO is located on one (for SiW_{10} -APTES) or two (P_2W_{17} -APTES) amines of the APTES part, while the LUMO are localized on the W atoms of the POM part. By grafting the B_{10} clusters, the LUMO levels are slightly affected. LUMO remains localized on W atoms and only minor changes are observed.

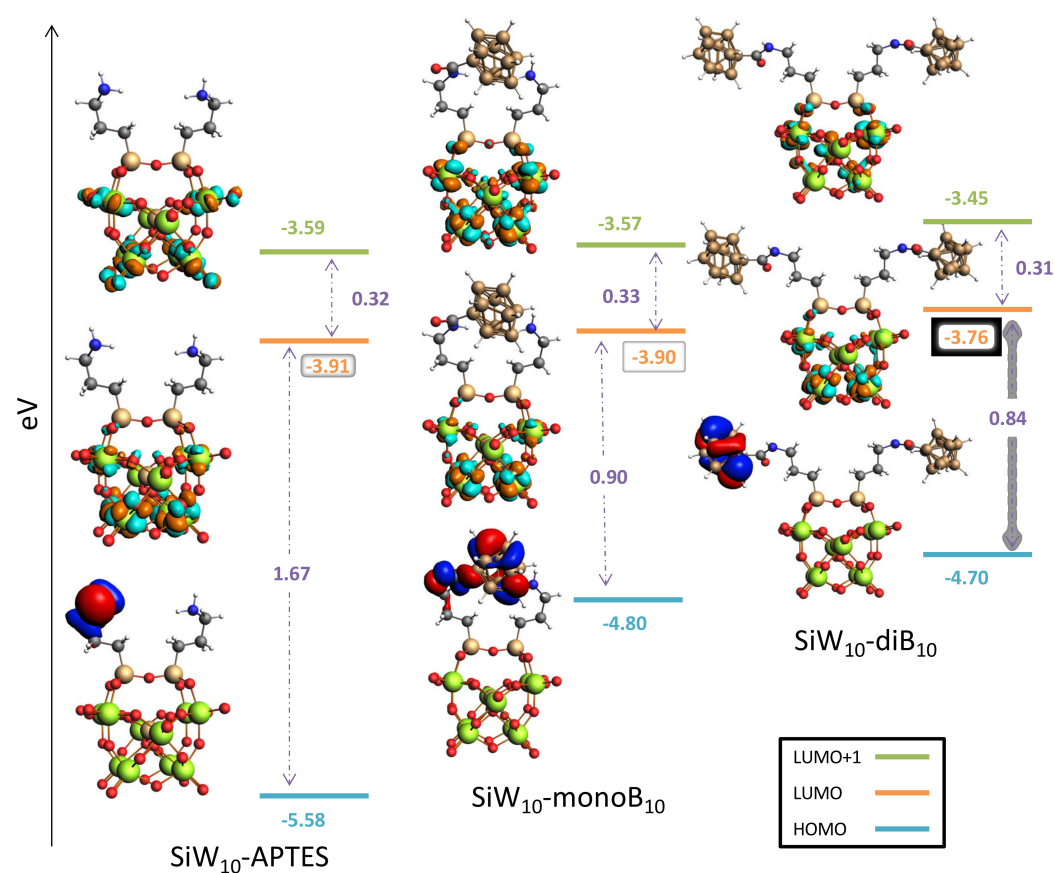


Figure 9. Frontier orbitals energies and energy gaps (eV) for the SiW_{10} -APTES, SiW_{10} -monoB₁₀ and SiW_{10} -diB₁₀ species. Color code: W green, O red, Si light brown, B dark brown, C grey, N blue, H white; HOMO: red/blue; LUMO: orange/cyan. MO surfaces plotted at a 0.03 isovalue.

Conversely, the HOMO levels are drastically modified by the introduction of B_{10} clusters. Electrons of the HOMO orbitals are now mainly localized on one grafted B_{10} cluster. Interestingly, for SiW_{10} -monoB₁₀ the HOMO is delocalized between one B_{10} cluster and the amine of the second arm, which strongly interacts with the B_{10} through H-H contacts. The HOMO energy level increases in all cases within the range 0.78 to 0.92 eV. The HOMO-LUMO gaps, are thus significantly reduced upon the B_{10} grafting. Indeed, for SiW_{10} -APTES, the gap decreases from 1.67 to 0.90 eV for the first substitution, and to 0.94 eV for the second. For P_2W_{17} -APTES, the gap evolves from 1.56 to 0.77 eV for the first substitution, and to 0.76 eV for the second.

2.6. Electrochemical Properties

The electronic spectra of compounds SiW_{10} -monoB₁₀, SiW_{10} -diB₁₀ and P_2W_{17} -diB₁₀ recorded in CH_3CN containing 0.1 mol.L^{-1} TBAClO₄ (TBAP, tetrabutylammonium perchlorate)

at room temperature and 2.10^{-4} mol.L $^{-1}$ concentration are depicted in Figures S35 and S36 (Supplementary Materials).

The electronic spectra of precursors **SiW₁₀-APTES** and **P₂W₁₇-APTES** display absorption bands in ultraviolet region corresponding to transition between p-orbitals of the oxo ligands and d-type orbitals centered on tungsten [33,34], while the cluster **[B₁₀H₉CO] $^{-}$** exhibits weak absorption band between 300 and 200 nm notably assigned to $\pi-\pi^*$ transitions [35]. Considering that the main contribution of the spectra comes from the LMCT band involving the W atoms and that the LUMO band centered on tungsten atoms are only slightly modified upon grafting of B₁₀ cluster, no drastic changes are expected in the POM-B₁₀ adducts. Indeed, the electronic spectra of **SiW₁₀-monoB₁₀** and **P₂W₁₇-diB₁₀** match well with the sum of the spectra of **SiW₁₀-APTES** or **P₂W₁₇-APTES** and one or two times that of **[B₁₀H₉CO] $^{-}$** , respectively. The spectrum of **SiW₁₀-diB₁₀** slightly differs from the sum of the component's spectra probably due to a larger variation of LUMO energy level from **SiW₁₀-APTES** to **SiW₁₀-diB₁₀** and additional constraints due to the vicinity of the two boron clusters.

Since no evolution of the spectra were observed within 24 h in such a medium, the compounds appear chemically stable in these experimental conditions. The cyclic voltammograms (CVs) were thus recorded for all the SiW₁₀ and P₂W₁₇ derivatives and are given in Figure 10 and in Figures S37 and S38 (Supplementary Materials), while the anodic and cathodic potentials are gathered in Table S3 (Supplementary Materials).

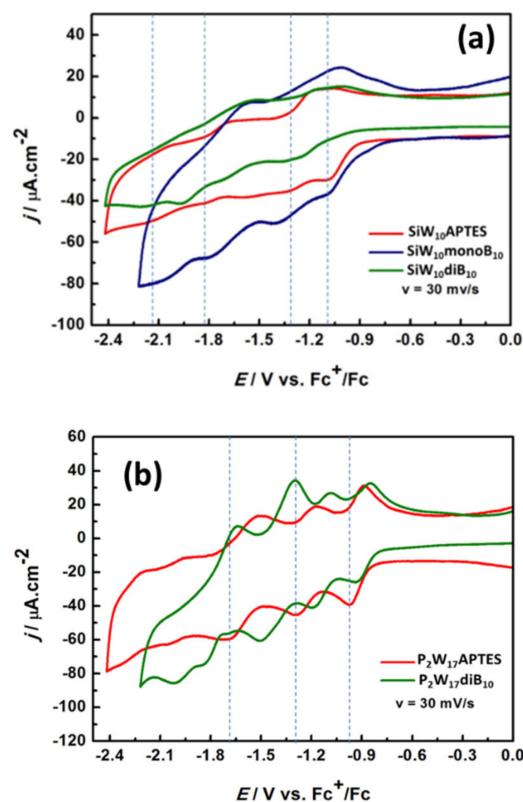


Figure 10. Comparison of cyclic voltammograms (a) for the three compounds **SiW₁₀-APTES**, **SiW₁₀-monoB₁₀** and **SiW₁₀-diB₁₀**, and (b) for **P₂W₁₇-APTES** and **P₂W₁₇-diB₁₀** in the reduction part. The electrolyte was CH₃CN + 0.1 M TBAClO₄. Dashed lines are only guide for eyes.

As depicted in Figure 10a and Figure S37, the CV of **SiW₁₀-APTES** is poorly resolved and it is difficult to identify confidently all the reduction processes corresponding to the successive reduction in W^{VI} centers into W^V, well-known to be monoelectronic in non-aqueous solvents [36]. These waves seem nevertheless reversible with processes better resolved in oxidation. Besides, an irreversible process attributed to the oxidation of amine function of the APTES linker is also observed in oxidation around +0.452 V vs. Fc⁺/Fc

(see Supplementary Materials). As for their parent precursor, CVs of **SiW₁₀-monoB₁₀** and **SiW₁₀-diB₁₀** display poorly resolved reversible electronic transfers, which appear shifted towards more negative potentials and one irreversible oxidation process around +0.452 V vs. Fc⁺/Fc assigned to the oxidation of the remaining amine function and/or of the B₁₀ cluster (see Figure S39, Supplementary Materials). This behavior agrees with the increase in the charge from 4- in **SiW₁₀-APTES** to 6- in **SiW₁₀-monoB₁₀** and 8- in **SiW₁₀-diB₁₀** and the electron donating character of the boron cluster [37] but does not evidence a strong electronic effect of the boron cluster on the POMs electronic properties.

The CVs of **P₂W₁₇-APTES** and **P₂W₁₇-diB₁₀** are given in Figure 10b and in Figure S38 (Supplementary Materials) and appears much more resolved than those of SiW₁₀ derivatives. The CV of **P₂W₁₇-APTES** displays four reversible electronic transfers with cathodic peak potentials assigned to successive mono- or bi-electronic reductions of W^{VI} centers into W(+V) [38] and two irreversible oxidation processes at E_{pa} = +0.452 and +0.759 V, assigned to the oxidation of the terminal amine groups of the APTES linkers. Conversely to the di-adduct compound **SiW₁₀-diB₁₀**, the CVs of the Dawson derivative **P₂W₁₇-diB₁₀** give four reversible reduction processes significantly shifted towards the more positive potential compared to **P₂W₁₇-APTES** and one irreversible reduction process at E_{pc} = -2.030 V vs. Fc⁺/Fc, which was not observed in the precursor. The opposite effect was expected. This effect probably results from a combination of a charge effect, the presence of protons (in DIPEAH⁺ cations) and of an electronic effect of boron cluster on P₂W₁₇ moiety but at this stage it is difficult to have a clear explanation of the contribution of all these effects which can be antagonist.

Although reduction waves in the Dawson derivatives are not very well resolved, it can be observed that the di-substituted species (green line in Figure 10) is reduced at lower potentials than **P₂W₁₇-APTES**, in agreement with the fact that the LUMO and LUMO+1 raise in energy upon B₁₀ attachment. Also, the successive reduction waves seem just shifted left, which would conform with the almost constant difference in the LUMO and LUMO+1 energies along the series.

2.7. Electrocatalytic Properties for the Reduction in Protons into Hydrogen (HER)

Many POMs are known to catalyze protons reduction into hydrogen in aqueous or in non-aqueous conditions [7,39,40]. We verified by UV-Vis spectroscopy that [B₁₀H₉CO]⁻ and its adducts with POMs are stable in CH₃CN in the presence of excess acetic acid (20 equivalents). In these conditions, it was interesting to study the reactivity of these compounds in regard to the electro-catalytic reduction in protons into hydrogen. The experiments were performed in CH₃CN + 0.1 M TBAP by using acetic acid as a source of protons, and as a weak acid in such a medium (pK_a = 22.3) [41].

Figure 11 and Figure S40 (Supplementary Materials) show the evolution of CVs upon stepwise addition of acetic acid up to 20 equivalents of acid/POM for all P₂W₁₇ and SiW₁₀ derivatives, respectively. For all the compounds, the addition of acetic acid, gives a new irreversible reduction wave, which grows gradually with the amount of acid, expressed as $\gamma = [\text{acid}]/[\text{POM}]$. As shown in Figure 11 and Figure S40, at a given potential of -2.2 V vs Fc⁺/Fc, a linear dependence of the catalytic current versus γ is obtained, a behavior featuring the electro-catalytic reduction of protons. However, the effect of the addition of acetic acid in the solution appears stronger for P₂W₁₇ derivatives than for SiW₁₀ based compounds.

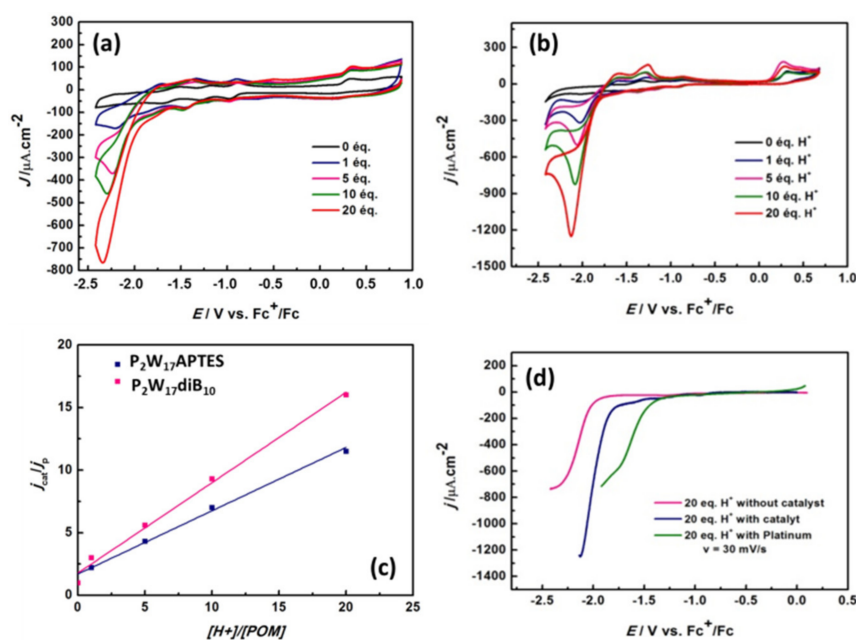


Figure 11. Cyclic voltammograms of (a) P_2W_{17} -APTES and (b) P_2W_{17} -diB10 after addition of variable amounts of acetic acid. (c) Plots of the cathodic currents measured at -2.2 V vs Fc^+/Fc as a function of the ratio $[acid]/[POM]$ for P_2W_{17} -APTES and P_2W_{17} -diB10. (d) Comparison of HER with and without catalyst P_2W_{17} -diB10, and with platinum after addition of an excess of acetic acid corresponding to the quantity added for a ratio $[acid]/[POM] = 20$. In all cases, the electrolyte was $CH_3CN + 0.1$ M $TBAClO_4$. The reference electrode was a saturated calomel electrode (SCE). Reproduced with permission from the doctoral thesis manuscript of Dr Manal Diab, University Paris Saclay/Lebanese University, May 2018.

To evidence the electrocatalytic process, linear voltammetry of P_2W_{17} -diB10 in the presence of 20 equivalents of acetic acid was performed and compared to similar experiments performed without catalyst or on platinum electrode (Figure 11d). We notice that in the presence of the catalyst P_2W_{17} -diB10, the current density is almost doubled and there is a 250-mV overvoltage decrease compared to the solution without catalyst. Indeed, the proton reduction with respect to platinum starts at -1.400 V vs. Fc^+/Fc , while it starts at -1.750 V vs. Fc^+/Fc with catalyst and at -2.000 V vs. Fc^+/Fc without catalyst. Finally, the formation of hydrogen is unambiguously demonstrated by gas chromatography analysis during electrolysis performed at -2.200 V vs Fc^+/Fc during 4.5 h (Figure S40, Supplementary Materials).

To compare the efficiency of all compounds, the catalytic efficiency (CAT) can be estimated using Equation (1):

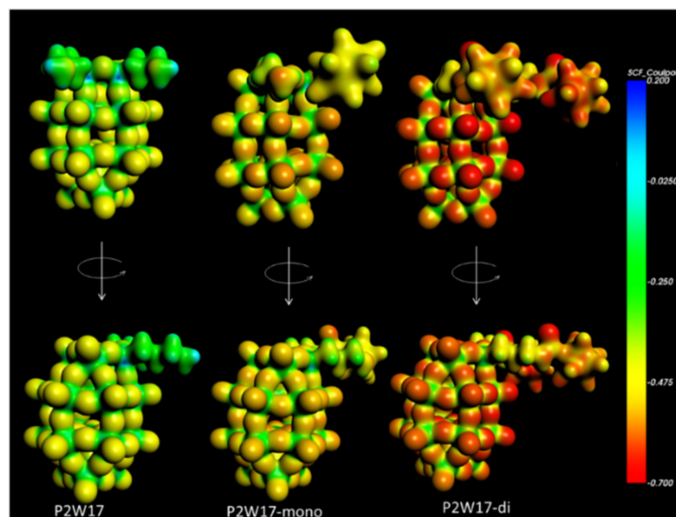
$$CAT = \frac{100 * (J_{(POM+20\ eq.\ CH_3COOH)} - J_{(POM\ alone)})}{J_{(POM\ alone)}} \quad (1)$$

Table 1 summarizes the CAT values measured for our products at -2.2 V vs Fc^+/Fc . Interestingly, the two precursors SiW_{10} -APTES and P_2W_{17} -APTES exhibit similar efficiency. Also, the efficiency of SiW_{10} -monoB10 and SiW_{10} -diB10 adducts are lower than that of SiW_{10} -APTES, while it is the opposite for P_2W_{17} -diB10, which appears much more efficient than its parent precursor, in agreement with cyclic voltammetry experiments. Indeed, a less negative reduction potential of the POM part should facilitate the electro-catalytic reduction in protons.

Table 1. Electrocatalytic efficiency for the reduction of protons into hydrogen at $E = -2.2$ V vs. Fc+/Fc for 20 equivalents of CH_3COOH added in CH_3CN .

Compound	Catalytic Efficiency (%)
SiW₁₀-APTES	827
SiW₁₀-monoB₁₀	524
SiW₁₀-diB₁₀	548
P₂W₁₇-APTES	854
P₂W₁₇-diB₁₀	1340

In terms of mechanism, three key steps have to be considered: the protonation, the reduction in the catalyst and the transfer of electron towards the protons to give dihydrogen. For protonation step, since catalysis is observed in all compounds, it must occur on the most basic sites, either on the oxo groups of the POM moiety, on the free amine groups in **SiW₁₀-APTES** and **P₂W₁₇-APTES** or on boron clusters for **SiW₁₀-diB₁₀** and **P₂W₁₇-diB₁₀**. DFT calculations evidence that the most nucleophilic sites are found on the oxo ligands of the POM parts which are consequently the preferential sites for protonation (see Figure 12 and Figure S34 in Supplementary Materials).

**Figure 12.** Two views of the molecular electrostatic potential in atomic units (a.u.) projected onto an electron density isosurface ($0.03 \text{ e}\cdot\text{au}^{-3}$) for **P₂W₁₇-APTES**, **P₂W₁₇-monoB₁₀** and **P₂W₁₇-diB₁₀** species.

For the reduction step, as seen in Figure S41c,d in Supplementary Materials, during electrolysis, the **P₂W₁₇** derivatives turned to blue as expected for the reduction in such species before returning back colorless when the current is stopped indicating that the reduced POM probably transfers electrons to protons to produce hydrogen. We understand well that if this reduction occurs at higher potential, it should favor the process. **P₂W₁₇-diB₁₀** is thus logically the most efficient compound.

To sum up, even if the decaborate cluster is probably not directly involved in the HER process, it plays two indirect roles: (1) the covalent grafting on POMs increases the electronic density on the POM which should facilitate the protonation step, and (2) the covalent grafting can modify the reduction potential of the POM moieties in POM-borate adducts, which favors the reduction step of the POM species when shifted towards more positive potentials as observed in **P₂W₁₇-diB₁₀**.

3. Conclusions

In this work, we succeeded in combining covalently the anionic $[\text{B}_{10}\text{H}_9\text{CO}]^-$ cluster with anionic **SiW₁₀** and **P₂W₁₇** derivatives using functionalized silyl derivatives (APTES) as a linker. The coupling between the two families of anionic parts appears much stronger

than that with Anderson-type POMs we previously reported [23] and detailed NMR study allowed establishing the optimized conditions for the synthesis of target compounds. Hence, the selective isolation of mono- and di-adduct compounds of boron cluster with **SiW₁₀-APTES**, namely [(SiW₁₀O₃₆)(B₁₀H₉CONHC₃H₆Si)(NH₂C₃H₆Si)O]⁶⁻ and [(SiW₁₀O₃₆)(B₁₀H₉CONHC₃H₆Si)₂O]⁸⁻ was successfully achieved, while only the di-adduct [(P₂W₁₇O₆₁)(B₁₀H₉CONHC₃H₆Si)₂O]¹⁰⁻ was isolated with **P₂W₁₇-APTES**. To the best of our knowledge, it is the first time that a mono-adduct can be isolated directly from the synthesis by functionalization of the **SiW₁₀-APTES** precursor. DFT studies supported by experimental NMR data evidenced that the formation of intramolecular H-H dihydrogen contact is the driving force for the preferred formation of the mono-adduct species and such a synthetic strategy could open the route toward the formation of hybrid POMs with two different functional groups.

All these compounds were fully characterized by multi-NMR techniques including ¹H, ¹¹B, ¹³C, ¹⁵N, ²⁹Si, ¹⁸³W and ³¹P as well as multi-dimensional correlations such as COSY, HMBC (¹H-¹³C and ¹H-¹⁵N) and ROESY NMR allowing focusing on each part of the adducts, i.e., POM, linker and boron cluster. These characterizations demonstrated unambiguously the formation of the targeted adducts and were also consistent with FT-IR and MALDI-TOF spectrometry data. DFT studies permitted to get optimized structures for all compounds consistent with the NMR data.

The electrochemical studies allowed studying the electronic effects of the grafting of the reducing boron cluster on some oxidized POMs with probable antagonist effect between charge effect and the variation of frontiers orbitals levels upon grafting of B₁₀ cluster. Finally, electro-catalytic reduction in protons into hydrogen was evidenced for these systems, the best efficiency being obtained with **P₂W₁₇-diB₁₀**. The process appears mainly effective on the POM part while the boron cluster participates only indirectly to the process.

Supplementary Materials: The following supporting information can be downloaded at: <https://www.mdpi.com/article/10.3390/molecules27227663/s1>. Experimental section including general methods, the ²⁹Si, ³¹P and ¹H NMR titration studies (Figures S1–S10) and the syntheses of compounds used in this study; FT-IR spectra (Figures S11 and S12); MALDI-TOF data (Table S1) and spectra (Figures S13–S16); a summary of NMR data (Table S2), ¹¹B NMR studies (Figures S17–S20), ²⁹Si NMR spectra (Figures S21 and S22), ³¹P NMR spectra (Figure S23), ¹H NMR studies including COSY, ROESY and ¹H-¹⁵N HMBC experiments (Figures S24–S29); ¹³C NMR studies (Figures S30–S32); a DFT part including computational details, frontiers orbitals of P₂W₁₇ derivatives (Figure S33) and electron density maps on SiW₁₀ derivatives (Figure S34); electronic spectra (Figures S35 and S36), additional cyclovoltammograms (Figures S37–S39) and table of potentials (Table S3); Evidence of the production of hydrogen and picture of the reduced POM during the HER process (Figures S40 and S41).

Author Contributions: Synthesis and solution studies, M.D. and Z.E.H.; elemental analyses, N.L.; supervision of NMR studies, M.H.; MALDI-TOF experiments, V.G. and D.T.; DFT Calculation, A.M. and C.B.; electrochemical studies, J.E.C. and A.R.; supervision of the work and funding acquisition, E.C., D.N. and S.F. All authors have read and agreed to the published version of the manuscript.

Funding: This research was funded by a public grant overseen by the French National Research Agency as part of the «Investissements d’Avenir» program (Labex Charm3at, ANR-11-LABX-0039-grat), by the Paris Ile-de-France Region-DIM “Respire”, and by a mobility program PHC CEDRE (project POMBORON n°42237UG). M.D. thanks AZM association and IUF for financial support and Z.E.H. thanks CampusFrance for Eiffel doctoral grant. We also thank CERCA Program of the Generalitat de Catalunya, the ICIQ Foundation, and the Spanish Ministerio de Ciencia e Innovación through project PID2020-112806RB-I00 and through the Severo Ochoa Excellence Accreditation 2020–2023 (CEX2019-000925-S, MCI/AEI).

Institutional Review Board Statement: Not applicable.

Informed Consent Statement: Not applicable.

Data Availability Statement: A data set collection of computational results is available in the ioChem-BD repository and can be accessed via <https://dx.doi.org/10.19061/iochem-bd-1-217> (accessed on 1 November 2022).

Acknowledgments: We acknowledge the Centre National de la Recherche Scientifique (CNRS) and the Ministère de l'Éducation Nationale de l'Enseignement Supérieur, de la Recherche et de l'Innovation (MESRI) for their financial support. This study results from an international collaboration supported by IRN-CNRS 2019–2023.

Conflicts of Interest: The authors declare no conflict of interest.

References

1. Lin, C.G.; Fura, G.D.; Long, Y.; Xuan, W.M.; Song, Y.F. Polyoxometalate-based supramolecular hydrogels constructed through host–guest interactions. *Inorg. Chem. Front.* **2017**, *4*, 789–794. [[CrossRef](#)]
2. Izzet, G.; Abecassis, B.; Brouri, D.; Piot, M.; Matt, B.; Serapian, S.A.; Bo, C.; Proust, A. Hierarchical Self-Assembly of Polyoxometalate-Based Hybrids Driven by Metal Coordination and Electrostatic Interactions: From Discrete Supramolecular Species to Dense Monodisperse Nanoparticles. *J. Am. Chem. Soc.* **2016**, *138*, 5093–5099. [[CrossRef](#)] [[PubMed](#)]
3. Zhu, Y.; Yin, P.C.; Xiao, F.P.; Li, D.; Bitterlich, E.; Xiao, Z.C.; Zhang, J.; Hao, J.T.; Liu, B.; Wang, Y.; et al. Bottom-Up Construction of POM-Based Macrostructures: Coordination Assembled Paddle-Wheel Macroclusters and Their Vesicle-like Supramolecular Aggregation in Solution. *J. Am. Chem. Soc.* **2013**, *135*, 17155–17160. [[CrossRef](#)] [[PubMed](#)]
4. Vickers, J.W.; Lv, H.J.; Sumliner, J.M.; Zhu, G.B.; Luo, Z.; Musaev, D.G.; Geletii, Y.V.; Hill, C.L. Differentiating Homogeneous and Heterogeneous Water Oxidation Catalysis: Confirmation that $[\text{Co}_4(\text{H}_2\text{O})_2(\alpha\text{-PW}_9\text{O}_{34})_2]^{10-}$ Is a Molecular Water Oxidation Catalyst. *J. Am. Chem. Soc.* **2013**, *135*, 14110–14118. [[CrossRef](#)] [[PubMed](#)]
5. Sarma, B.B.; Neumann, R. Polyoxometalate-mediated electron transfer–oxygen transfer oxidation of cellulose and hemicellulose to synthesis gas. *Nat. Commun.* **2014**, *5*, 4621. [[CrossRef](#)] [[PubMed](#)]
6. Natali, M.; Orlandi, M.; Berardi, S.; Campagna, S.; Bonchio, M.; Sartorel, A.; Scandola, F. Photoinduced Water Oxidation by a Tetraruthenium Polyoxometalate Catalyst: Ion-pairing and Primary Processes with $\text{Ru}(\text{bpy})_3^{2+}$ Photosensitizer. *Inorg. Chem.* **2012**, *51*, 7324–7331. [[CrossRef](#)]
7. Keita, B.; Nadjo, L. Polyoxometalate-based homogeneous catalysis of electrode reactions: Recent achievements. *J. Mol. Catal. A Chem.* **2007**, *262*, 190–215. [[CrossRef](#)]
8. Freire, C.; Fernandes, D.M.; Nunes, M.; Abdelkader, V.K. POM & MOF-based Electrocatalysts for Energy-related Reactions. *ChemCatChem* **2018**, *10*, 1703–1730.
9. Zhao, J.-W.; Li, Y.-Z.; Chen, L.-J.; Yang, G.-Y. Research progress on polyoxometalate-based transition-metal–rare-earth heterometallic derived materials: Synthetic strategies, structural overview and functional applications. *Chem. Commun.* **2016**, *52*, 4418–4445. [[CrossRef](#)]
10. Hasenknopf, B. Polyoxometalates: Introduction to a class of inorganic compounds and their biomedical applications. *Front. Biosci.* **2005**, *10*, 275–287. [[CrossRef](#)]
11. Yamase, T. Anti-tumor, -viral, and -bacterial activities of polyoxometalates for realizing an inorganic drug. *J. Mater. Chem.* **2005**, *15*, 4773–4782. [[CrossRef](#)]
12. Bijelic, A.; Aureliano, M.; Rompel, A. The antibacterial activity of polyoxometalates: Structures, antibiotic effects and future perspectives. *Chem. Commun.* **2018**, *54*, 1153–1169. [[CrossRef](#)] [[PubMed](#)]
13. Bijelic, A.; Aureliano, M.; Rompel, A. Polyoxometalates as Potential Next-Generation Metallodrugs in the Combat Against Cancer. *Angew. Chem. Int. Ed.* **2019**, *58*, 2980–2999. [[CrossRef](#)] [[PubMed](#)]
14. Sivaev, I.B.; Bregadze, V.I.; Kuznetsov, N.T. Derivatives of the closo-dodecaborate anion and their application in medicine. *Russ. Chem. Bull.* **2002**, *51*, 1362–1374. [[CrossRef](#)]
15. Zhu, Y.; Hosmane, N.S. Nanostructured boron compounds for cancer therapy. *Pure Appl. Chem.* **2018**, *90*, 653–663. [[CrossRef](#)]
16. Hey-Hawkins, E.; Viñas-Teixidor, C. *Boron-Based Compounds: Potential and Emerging Applications in Medicine*; John Wiley&Sons Ltd.: Hoboken, NJ, USA, 2018.
17. Hosmane, N.S. *Boron Science: New Technologies and Applications*; CRC Press: Boca Raton, FL, USA, 2012.
18. Zhu, Y.; Hosmane, N.S. Applications and perspectives of boron-enriched nanocomposites in cancer therapy. *Future Med. Chem.* **2013**, *5*, 705–714.
19. Sivaev, I.B.; Prikaznov, A.V.; Naoufal, D. Fifty years of the closo-decaborate anion chemistry. *Collect. Czechoslov. Chem. Commun.* **2010**, *75*, 1149–1199. [[CrossRef](#)]
20. Mahfouz, N.; Abi Ghaida, F.; El Hajj, Z.; Diab, M.; Floquet, S.; Mehdi, A.; Naoufal, D. Recent Achievements on Functionalization within closo-Decahydrodecaborate $[\text{B}_{10}\text{H}_{10}]^{2-}$ Clusters. *Chem. Sel.* **2022**, *7*, e202200770.
21. Abi-Ghaida, F.; Clement, S.; Safa, A.; Naoufal, D.; Mehdi, A. Multifunctional Silica Nanoparticles Modified via Silylated-Decaborate Precursors. *J. Nanomater.* **2015**, *2015*, 608432. [[CrossRef](#)]
22. Abi-Ghaida, F.; Laila, Z.; Ibrahim, G.; Naoufal, D.; Mehdi, A. New triethoxysilylated 10-vertex closo-decaborate clusters. Synthesis and controlled immobilization into mesoporous silica. *Dalton Trans.* **2014**, *43*, 13087–13095. [[CrossRef](#)]
23. Diab, M.; Mateo, A.; Al Cheikh, J.; Haouas, M.; Ranjbari, A.; Bourdreux, F.; Naoufal, D.; Cadot, E.; Bo, C.; Floquet, S. Unprecedented coupling reaction between two anionic species of a closo-decahydrodecaborate cluster and an Anderson-type polyoxometalate. *Dalton Trans.* **2020**, *49*, 4685–4689. [[CrossRef](#)] [[PubMed](#)]
24. Izzet, G.; Volatron, F.; Proust, A. Tailor-made Covalent Organic-Inorganic Polyoxometalate Hybrids: Versatile Platforms for the Elaboration of Functional Molecular Architectures. *Chem. Rec.* **2017**, *17*, 250–266. [[CrossRef](#)] [[PubMed](#)]

25. Proust, A.; Matt, B.; Villanneau, R.; Guillemot, G.; Gouzerh, P.; Izzet, G. Functionalization and post-functionalization: A step towards polyoxometalate-based materials. *Chem. Soc. Rev.* **2012**, *41*, 7605–7622. [[CrossRef](#)] [[PubMed](#)]
26. Piot, M.; Hupin, S.; Lavanant, H.; Afonso, C.; Bouteiller, L.; Proust, A.; Izzet, G. Charge Effect on the Formation of Polyoxometalate-Based Supramolecular Polygons Driven by Metal Coordination. *Inorg. Chem.* **2017**, *56*, 8490–8496. [[CrossRef](#)]
27. Shelly, K.; Knobler, C.B.; Hawthorne, M.F. Synthesis of monosubstituted derivatives of closo decahydrodecaborate(2-). X-ray crystal structures of [closo-2-B₁₀H₉CO][−] and [closo-2-B₁₀H₉NCO]^{2−}. *Inorg. Chem.* **1992**, *31*, 2889–2892. [[CrossRef](#)]
28. Mayer, C.R.; Fournier, I.; Thouvenot, R. Bis- and Tetrakis(organosilyl) Decatungstosilicate, [γ-SiW₁₀O₃₆(RSi)₂O]^{4−} and [γ-SiW₁₀O₃₆(RSiO)₄]^{4−}: Synthesis and Structural Determination by Multinuclear NMR Spectroscopy and Matrix-Assisted Laser Desorption/Desorption Time-of-Flight Mass Spectrometry. *R. Chem. Eur. J.* **2000**, *6*, 105–110. [[CrossRef](#)]
29. Bonchio, M.; Carraro, M.; Scorrano, G.; Bagnò, A. Photooxidation in Water by New Hybrid Molecular Photocatalysts Integrating an Organic Sensitizer with a Polyoxometalate Core. *Adv. Synth. Catal.* **2004**, *346*, 648–654. [[CrossRef](#)]
30. Modugno, G.; Monney, A.; Bonchio, M.; Albrecht, M.; Carraro, M. Transfer Hydrogenation Catalysis by a N-Heterocyclic Carbene (NHC) Iridium Complex on a Polyoxometalate Platform. *Eur. J. Inorg. Chem.* **2014**, *14*, 2356–2360. [[CrossRef](#)]
31. Carraro, M.; Modugno, G.; Fiorani, G.; Maccato, C.; Sartorel, A.; Bonchio, M. Organic-Inorganic Molecular Nano-Sensors: A Bis-Dansylated Tweezer-Like Fluorionophore Integrating a Polyoxometalate Core. *Eur. J. Org. Chem.* **2012**, 281–289. [[CrossRef](#)]
32. Mayer, C.R.; Roch-Marchal, C.; Lavanant, H.; Thouvenot, R.; Sellier, N.; Blais, J.C.; Sécheresse, F. New Organosilyl Derivatives of the Dawson Polyoxometalate [α₂-P₂W₁₇O₆₁(RSi)₂O]^{6−}: Synthesis and Mass Spectrometric Investigation. *Chem. Eur. J.* **2004**, *10*, 5517–5523. [[CrossRef](#)]
33. Maestre, J.M.; Lopez, X.; Bo, C.; Poblet, J.-M.; Daul, C. A DFT Study of the Electronic Spectrum of the α-Keggin Anion [Co^{II}W₁₂O₄₀]^{6−}. *Inorg. Chem.* **2002**, *41*, 1883–1888. [[CrossRef](#)] [[PubMed](#)]
34. Ravelli, D.; Dondi, D.; Fagnoni, M.; Albini, A.; Bagnò, A. Predicting the UV spectrum of polyoxometalates by TD-DFT. *J. Comput. Chem.* **2011**, *32*, 2983–2987. [[CrossRef](#)] [[PubMed](#)]
35. Pogula, L.P.; Ramakrishna, D.S. Charge Distribution and UV Absorption Spectra of Liquid Crystals with Structural Element [closo-B₁₀H₁₀]^{2−}: A Theoretical Approach. *IAR/JSET* **2015**, *2*, 92–95.
36. Kemmegne-Mbouguen, J.C.; Floquet, S.; Zang, D.; Bonnefont, A.; Ruhlmann, L.; Simonnet-Jégat, C.; López, X.; Haouas, M.; Cadot, E. Electrochemical properties of the [SiW₁₀O₃₆(M₂O₂E₂)]₆− polyoxometalate series (M = Mo(v) or W(v); E = S or O). *New J. Chem.* **2019**, *43*, 1146–1155.
37. Sivaev, I.B.; Prikaznov, A.V.; Anufriev, S.A. On relative electronic effects of polyhedral boron hydrides. *J. Organomet. Chem.* **2013**, *747*, 254–256. [[CrossRef](#)]
38. Boujita, M.; Boixel, J.; Blart, E.; Mayer, C.R.; Odobel, F. Redox properties of hybrid Dawson type polyoxometalates disubstituted with organo-silyl or organo-phosphoryl moieties. *Polyhedron* **2008**, *27*, 688–692. [[CrossRef](#)]
39. Liu, R.J.; Zhang, G.J.; Cao, H.B.; Zhang, S.J.; Xie, Y.B.; Haider, A.; Kortz, U.; Chen, B.H.; Dalal, N.S.; Zhao, Y.S.; et al. Enhanced proton and electron reservoir abilities of polyoxometalate grafted on graphene for high-performance hydrogen evolution. *Energy Environ. Sci.* **2016**, *9*, 1012–1023. [[CrossRef](#)]
40. Keita, B.; Kortz, U.; Holzle, L.R.B.; Brown, S.; Nadjò, L. Efficient Hydrogen-Evolving Cathodes Based on Proton and Electron Reservoir Behaviors of the Phosphotungstate [H₇P₈W₄₈O₁₈₄]^{33−} and the Co(II)-Containing Silicotungstates [Co₆(H₂O)₃₀{Co₉Cl₂(OH)₃(H₂O)₉(β-SiW₈O₃₁)₃}]^{5−} and [Co₃(B-β-SiW₉O₃₃(OH))(B-β-SiW₈O₂₉(OH)₂)₂]^{22−}. *Langmuir* **2007**, *23*, 9531–9553.
41. Fourmond, V.; Jacques, P.A.; Fontecave, M.; Artero, V. H₂ evolution and molecular electrocatalysts: Determination of overpotentials and effect of homoconjugation. *Inorg. Chem.* **2010**, *49*, 10338–10347. [[CrossRef](#)]